SAND2018-3446J

Radial Inertia Effect on Dynamic Compressive Response of Polymeric Foam Materials

Bo Song[1], Brett Sanborn[1], Wei-Yang Lu[2]

[1] Sandia National Laboratories, Albuquerque, NM 87122

[2] Sandia National Laboratories, Livermore, CA 94551

Abstract

Polymeric foams have been extensively used in shock isolation applications because of their superior shock or impact energy absorption capability. To meet certain desired shock isolation requirements, the polymeric foams need to be experimentally characterized to obtain their intrinsic material response. However, radial inertia during dynamic compression has become a severe issue and needs to be fully understood. In this study, we developed an analytical method to calculate the additional stress induced by radial inertia in a polymeric foam specimen. The radial inertia is generally caused by Poisson's effect and associated with three different mechanisms – axial strain acceleration, large deformation, and Poisson's ratio change. The effect of Poisson's ratio change during deformation on radial inertia was specifically investigated for hyperelastic foam materials, and verified with experimental results obtained from Kolsky compression bar tests on a silicone foam.

Keywords: Radial inertia, Poisson's ratio, dynamic response, polymeric foam, split Hopkinson pressure bar (SHPB), Kolsky bar

1. Introduction

Polymeric foams have been extensively used in shock isolation applications because of their superior shock or impact energy absorption capability [1-4]. To meet certain desired shock isolation requirements, the polymeric foams need to be experimentally characterized and numerically modeled in terms of material response under shock/impact loading and then evaluated with experimental, analytical, and/or numerical efforts. Dynamic compressive stress-strain response of polymeric foams is fundamental to the shock isolation performance.

In the past, polymeric foams have been dynamically characterized with split Hopkinson pressure bars, also called Kolsky compression bars, at various strain rates, temperatures, and stress states [5-8]. A typical Kolsky compression bar for polymeric foam testing is schematically shown in Fig. 1. There are challenges when the Kolsky compression bar shown in Fig. 1 is used to obtain dynamic compressive stress-strain response of polymeric foams. Due to the nature of low strength, stiffness, and wave speed in the polymeric foams, it is difficult to measure the weak transmitted signal, facilitate uniform deformation and stress equilibrium in a polymeric foam specimen when conducting Kolsky compression bar tests [9]. Highly sensitive transmission bar material, i.e., aluminum or polymer bars, and/or strain gage/force transducers are needed to detect the weak transmitted signal through the soft polymeric foam specimen [9-11]. A thin specimen and proper

pulse shaping have been demonstrated to facilitate uniform deformation and stress equilibrium during a Kolsky compression bar test [9-11].

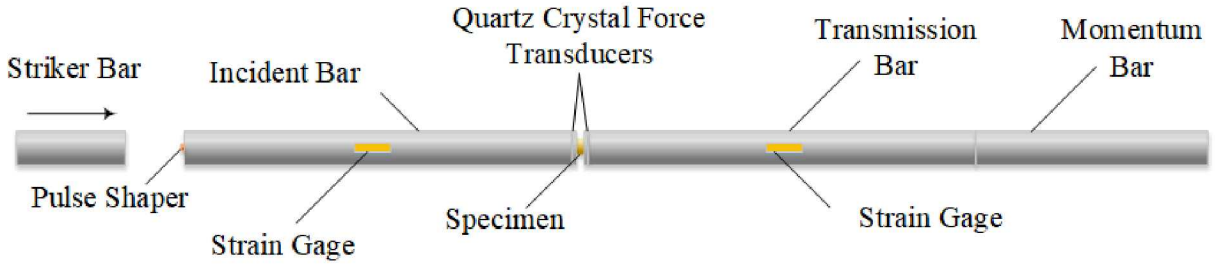

Figure 1. Schematic of Kolsky compression bar for dynamic compressive testing of polymeric foams

Radial inertia is another critical issue in characterization of very soft materials with a Kolsky compression bar [12, 13]. When a specimen is subjected to axial compressive loading in a Kolsky compression bar test, the specimen becomes radially expanded due to Poisson's effect. For a cylindrical specimen with initial dimensions of radius, a_0, and length, l_0, as shown in Fig. 2, Dharan and Hauser [14] presented a relationship between the axial and radial velocities to which an incompressible solid specimen is subjected,

$$V_r(t) = \frac{r}{2l} V_x(t) \tag{1}$$

where V_r and V_x are velocities in radial and axial directions, respectively; r and l are arbitrary radius in the specimen and thickness of the specimen at any time, respectively. Equation (1)

indicates that, even for a constant axial velocity V_x, the lateral velocity V_r increases with increasing axial strain or decreasing specimen thickness l when in compression. The increasing lateral velocity V_r results in an acceleration of the specimen material in the radial direction, which is called "radial inertia". The radial inertia produces an artificial radial confinement to the specimen, which results in additional axial stress to the specimen. The additional radial-inertia-induced axial stress does not represent the intrinsic uniaxial material response and must be corrected or removed.

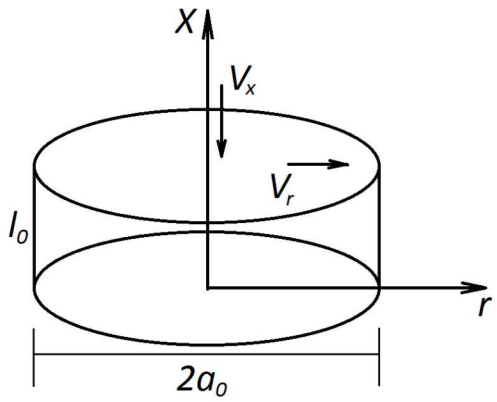

Figure 2. A cylindrical specimen under dynamic axial compression

Back to 1949, Kolsky [15] used an energy method to calculate the additional axial stress caused by the radial inertia,

$$\sigma_z = \frac{\nu^2 a_0^2 \rho_0}{2} \cdot \ddot{\varepsilon} \tag{2}$$

where a_0 is the radius of specimen; ν and ρ_0 are Poisson's ratio and density of the specimen material, respectively; e is the axial engineering strain in the specimen. Forrestal et al. [16] developed closed-form equations for the additional axial stress induced by radial inertia in linear elastic samples,

$$\sigma_z = \frac{\nu^2(3-2\nu)}{4(1-\nu)}\left[a_0^2 - \frac{2r^2}{(3-2\nu)}\right]\rho_0 \cdot \ddot{\varepsilon} \tag{3}$$

For an incompressible solid, $\nu = \frac{1}{2}$, Equation (3) becomes

$$\sigma_z(r) = \frac{\left(a^2 - r^2\right)}{4}\rho_0 \cdot \ddot{\varepsilon} \tag{4}$$

Integrating Equation (4) yields the average additional axial stress,

$$\bar{\sigma}_z = \frac{1}{\pi a^2}\int_0^a \int_0^{2\pi} \sigma_z(r) r dr d\theta \tag{5}$$

which gives the same result as Equation (2).

Radial inertia effects have been identified in studies of a variety of materials. Radial inertia-induced confinement has been concluded to be a contributor to strain rate effects in brittle materials. For example, Li and Meng [17] used numerical simulation to confirm that the apparent increase in dynamic strength of concrete-like materials in a Kolsky compression bar test was caused by lateral inertia. Holland and McMeeking [18] concluded that radial inertia-induced confinement was one of the mechanisms causing the increase in fracture strength of ceramics at high strain rates. Radial inertia has also been found by Rubin et al. [19] to stabilize the localization process on the inception of necking in a ductile metallic rod. Furthermore, the radial inertia effect was observed to be more significant in dynamic characterization of compressive stress-strain

response of soft materials including rubbers and biological tissues [12, 13, 20]. The radial-inertia-induced confinement resulted in an early spike in the dynamic compressive stress-strain curve of the soft materials. The amplitude of the stress spike was estimated to be on the order of 1 MPa, which is not negligible for the materials with yield and flow stresses on the same order.

Numerical correction and experimental approaches have been proposed to minimize or remove the radial inertia effect [12, 21]. The additional axial stress caused by the radial inertia can be calculated with Equation (2) and then subtracted from the measured stress-strain response. In addition, Equation (4) suggests that the additional radial-inertia-induced axial stress has a parabolic distribution over the specimen radius with the maximum value at the center and zero at the cylindrical surface of the specimen. Therefore, using an annular specimen geometry can effectively minimize the radial inertia effect, which has been proved for soft polymers, biological tissues, and concrete-like materials [12, 21]. Equations (2) and (4) also indicate that constant strain rate could remove the radial inertia effect, which is inconsistent with the conclusion drawn by Dharan and Hauser [14]. In fact, Dharan and Hauser [14] presented the additional stress induced by radial inertia for an incompressible solid based on von Mises plasticity theory,

$$\bar{\sigma}_z = \frac{\rho_0 a_0^{\,2}}{4l_0\left(1-e_x\right)^2}\left[\frac{3V_x^2}{2l_0\left(1-e_x\right)}+\frac{dV_x}{dt}\right] \tag{6}$$

Warren and Forrestal [23] used similar methods to obtain the same equation in terms of additional stress as Equation (6). They also applied strain rate

$$\dot{\varepsilon}_x = \frac{V_x}{l_0} \tag{7}$$

to Equation (6) and the average radial-inertia-induced axial stress becomes

$$\bar{\sigma}_z = \frac{3\rho_0 a_0^{\,2}}{16\left(1-e_x\right)^3}\dot{\varepsilon}_x + \frac{\rho_0 a_0^2}{8\left(1-e_x\right)^2}\ddot{\varepsilon}_x \tag{8}$$

In a Kolsky compression bar test, strain rate ramps up before a constant rate (on the order of 10^3 s^{-1}) is reached. However, the ramping time for the strain rate is very short (usually less than 100 microseconds) such that the first term in Equation (8) is approximately one order in magnitude lower than the second term when the specimen is subjected to small deformation, making Equation (8) consistent with Equation (2). This indicates that Equation (2) and (4) are valid for an incompressible solid subjected to small deformation. When strain rate reaches a constant, the second term in Equation (8) vanishes and radial-inertia-induced stress is dominated by the first term only. This means the radial inertia would not be fully removed only by facilitating constant strain rate. Instead, the amplitude of the additional stress caused by radial inertia significantly increases with increasing strain.

As mentioned earlier, currently existing analyses of radial inertia effect assume of either incompressible solids or compressible solids with constant Poisson's ratios, which are not applicable to foam materials. Foam materials usually possess very small Poisson's ratio before densification. This small, or even nearly zero, Poisson's ratio does not generate radial inertia in the foam specimen when subjected to dynamic axial loading. Therefore, radial inertia can be neglected in a Kolsky compression bar test on a foam specimen prior to densification. However, when foam specimen is densified, the Poisson's ratio may be drastically changed from nearly zero to nearly incompressible ($\nu = \frac{1}{2}$). This drastic change in Poisson's ratio results in a sudden confinement to the specimen during densification process, which has not been incorporated in previous analyses. Therefore, it is desirable to understand the radial inertia effect on polymeric foams subjected to large deformation (passing densification) at high strain rates.

In this paper, we develop an analytical method to calculate the additional axial stress induced by radial inertia in a polymeric foam specimen. The effect of changing profile of Poisson's ratio during deformation on radial inertia is investigated and verified with experimental results obtained from Kolsky compression bar tests on a silicone foam.

2. Radial Inertia in a Compressible Cylindrical Solid

In this study a cylindrical specimen configuration shown in Fig. 2 is used for radial inertia analysis. An axial compression at velocity $V_x = V_x(t)$ generates a radial expansion with the velocity, $V_r = V_r(r,t)$. From mass conservation, we have

$$dm(t) = \pi \cdot d\left[\rho(t) \cdot r^2(t) \cdot l(t)\right] = 0 \tag{9}$$

where *m* is a constant mass; ρ is density, $\rho = \rho(t)$. Applying $dr(t) = V_r(r,t)dt$ and $dl(t) = V_x(t)dt$ Equation (9) can be expanded as

$$\frac{1}{\rho(t)} \cdot \frac{d\rho(t)}{dt} = -\left(\frac{V_x(t)}{l(t)} + 2\frac{V_r(r,t)}{r(t)} \right) \tag{10}$$

which shows density change of the specimen during axial compressive deformation. Equation (10) can also be rewritten as

$$V_r(r,t) = -\frac{r}{2}\left(\frac{V_x(t)}{l(t)} + \frac{d\ln\rho(t)}{dt} \right) \tag{11}$$

Differentiating Equation (11) yields

$$\frac{\partial V_r(r,t)}{\partial t} = -\frac{r}{2}\left[-\frac{V_x^2(t)}{l^2(t)} + \frac{1}{l(t)} \cdot \frac{dV_x(t)}{dt} + \frac{d^2\ln\rho(t)}{dt^2} \right] \tag{12}$$

$$\frac{\partial V_r(r,t)}{\partial r} = -\frac{1}{2}\left(\frac{V_x(t)}{l(t)} + \frac{d\ln\rho(t)}{dt}\right) \tag{13}$$

For a compressible solid with a Poisson's ratio, ν, the volume and density changes during deformation can be expressed as

$$\frac{d\Omega(t)}{\Omega(t)} = -\frac{d\rho(t)}{\rho(t)} = (1-2\nu(t))\frac{dl(t)}{l(t)} \tag{14}$$

where $\Omega(t)$ is time-dependent volume. Considering positive in compression, the specimen axial strain is defined as

$$e_x(t) = 1 - \frac{l(t)}{l_0} \tag{15}$$

Therefore,

$$d\ln\rho(t) = (1-2\nu(t))\frac{de_x(t)}{1-e_x(t)} \tag{16}$$

or

$$\frac{d\ln\rho(t)}{dt} = (1-2\nu(t))\frac{\dot{e}_x(t)}{1-e_x(t)} \tag{17}$$

Differentiating Equation (17) yields

$$\frac{d^2\ln\rho(t)}{dt^2} = (1-2\nu(t))\left[\frac{\ddot{e}_x(t)}{1-e_x(t)} + \frac{\dot{e}_x^2(t)}{(1-e_x(t))^2}\right] - 2\frac{d\nu(e_x)}{de_x}\cdot\frac{\dot{e}_x^2(t)}{1-e_x(t)} \tag{18}$$

Since strain rate is defined as

$$\dot{e}_x(t) = -\frac{V_x(t)}{l_0} \tag{19}$$

Therefore,

$$\frac{V_x(t)}{l(t)} = -\frac{\dot{e}_x(t)}{1-e_x(t)} \tag{20}$$

Applying Equations (17), (18), and (20) into (11), (12) and (13), we have

$$V_r(r,t) = r \cdot \nu(t) \cdot \frac{\dot{e}_x(t)}{1-e_x(t)} \tag{21}$$

$$\frac{\partial V_r(r,t)}{\partial t} = \frac{r}{1-e_x(t)}\left[\nu(t)\ddot{e}_x(t) + \nu(t)\cdot\frac{\dot{e}_x(t)}{1-e_x(t)} + \frac{d\nu(e_x)}{de_x}\dot{e}_x(t)\right] \tag{22}$$

$$\frac{\partial V_r(r,t)}{\partial r} = \nu(t)\frac{\dot{e}_x(t)}{1-e_x(t)} \tag{23}$$

From momentum conservation along radial direction, we have [23]

$$\frac{\partial T_{rr}(r,t)}{\partial r} + \frac{1}{r}\left(T_{rr}(r,t) - T_{\theta\theta}(r,t)\right) = -\rho\left(\frac{\partial V_r(r,t)}{\partial t} + V_r(r,t)\frac{\partial V_r(r,t)}{\partial r}\right) \tag{24}$$

where T_{rr} and $T_{\theta\theta}$ are the components of Cauchy stress in cylindrical coordinates. Under homogeneous deformation, the components are expressed as

$$T_{xx}(r,t) = \sigma_x(t) + \sigma_r(r,t) \tag{25}$$

$$T_{rr}(r,t) = T_{\theta\theta}(r,t) = \sigma_r(r,t) \tag{26}$$

where T_{xx} is the component of Cauchy stress along axial loading direction; $\sigma_r(r,t)$ is the radial stress due to inertia along radial direction. The radial stress here is considered as a hydrostatic stress due to particle acceleration [22, 24]. Substituting Equations (25) and (26) into (24), we have

$$\frac{\partial \sigma_r(r,t)}{\partial r} = -\rho(t)\left(\frac{\partial V_r(r,t)}{\partial t} + V_r(r,t)\frac{\partial V_r(r,t)}{\partial r}\right) \tag{27}$$

Therefore, applying Equations (21), (22), and (23) into (27) yields

$$\frac{\partial \sigma_r(r,t)}{\partial r} = -\rho(t)\cdot\frac{r}{1-e_x(t)}\cdot\left[\nu(t)\ddot{e}_x(t) + \nu(t)\cdot(\nu(t)+1)\cdot\frac{\dot{e}_x(t)}{1-e_x(t)} + \frac{d\nu(e_x)}{de_x}\dot{e}_x(t)\right] \tag{28}$$

Equation (28) integrates to

$$\sigma_r(r,t) = -\rho(t)\cdot\frac{r^2}{2(1-e_x(t))}\cdot\left[\nu(t)\ddot{e}_x(t) + \nu(t)\cdot(\nu(t)+1)\frac{\dot{e}_x(t)}{1-e_x(t)} + \frac{d\nu(e_x)}{de_x}\dot{e}_x(t)\right] + C \tag{29}$$

where C is an integral constant and determined with the boundary condition $\sigma_r(r,t)\big|_{r=a} = 0$,

$$C = \rho(t)\cdot\frac{a^2(t)}{2(1-e_x(t))}\cdot\left[\nu(t)\ddot{e}_x(t) + \nu(t)\cdot(\nu(t)+1)\frac{\dot{e}_x(t)}{1-e_x(t)} + \frac{d\nu(e_x)}{de_x}\dot{e}_x(t)\right] \tag{30}$$

Therefore, the radial-inertia-induced stress is expressed as

$$\sigma_r(r,t) = \rho(t)\cdot\frac{a^2(t)-r^2(t)}{2(1-e_x(t))}\cdot\left[\nu(t)\ddot{e}_x(t) + \nu(t)\cdot(\nu(t)+1)\frac{\dot{e}_x(t)}{1-e_x(t)} + \frac{d\nu(e_x)}{de_x}\dot{e}_x(t)\right] \tag{31}$$

Equation (31) indicates that the radial inertia effect includes three parts induced by 1) strain acceleration (the first term in the bracket in Eq. (31)); 2) large strain (the second term in the bracket

in Eq. (31)); and 3) change of Poisson's ratio (the third term in the bracket in Eq. (31). These three parts usually do not necessarily play equal roles in the radial-inertia-induced axial stress. Instead, the radial inertia stress can be dominated by some or all three depending on specific loading condition and specimen deformation process.

3. Discussion

3.1 Radial inertia in an incompressible solid

For an incompressible solid, $\nu = \frac{1}{2}$, we have

$$r^2(t) \cdot l(t) = r_0^2 \cdot l_0 \tag{32}$$

or

$$r(t) = \frac{r_0}{\sqrt{1 - e_x(t)}} \tag{33}$$

$$a(t) = \frac{a_0}{\sqrt{1 - e_x(t)}} \tag{34}$$

Equation (31) is simplified as

$$\sigma_r(r_0, t) = \rho_0 \cdot \frac{a_0^2 - r_0^2}{4\left(1 - e_x(t)\right)^2} \cdot \left[\ddot{e}_x(t) + \frac{3}{2} \cdot \frac{\dot{e}_x^2(t)}{1 - e_x(t)} \right] \tag{35}$$

Equation (35) has the exactly same form as the equation given by Warren and Forrestal [22]. The average engineering stress generated by radial inertia can thus be calculated as

$$\bar{\sigma}_r(t) = \frac{1}{\pi a_0^2}\int_0^{a_0} 2\pi r \sigma_r(r_0, t) dr_0 \tag{36}$$

and

$$\bar{\sigma}_r(t) = \frac{\rho_0^2 \cdot a_0^2}{8\left(1-e_x(t)\right)^2} \cdot \left[\ddot{e}_x(t) + \frac{3}{2} \cdot \frac{\dot{e}_x^2(t)}{1-e_x(t)}\right] \tag{37}$$

Equation (37) suggests that the additional axial stress caused by radial inertia depends on specimen strain, e_x, strain rate, $\dot{e}_x$, and strain acceleration, $\ddot{e}_x$, in addition to material/specimen constants, i.e. density, ρ_0, and initial radius, a_0. The additional stress caused by radial inertia can also be normalized as

$$\frac{\bar{\sigma}_r(e_x)}{\rho_0 a_0^2} = \frac{1}{8} \cdot \frac{1}{\left(1-e_x\right)^2} \cdot \left[\ddot{e}_x + \frac{3}{2} \cdot \frac{\dot{e}_x^2}{1-e_x}\right] \tag{38}$$

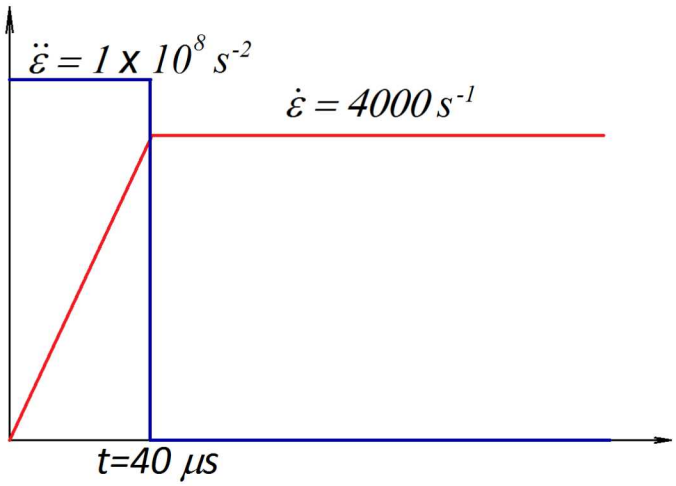

Figure 3. Strain-rate time history

Pulse shaping techniques have been extensively employed to achieve a constant strain rate in a Kolsky compression bar test. However, it still takes time for strain rate to reach a constant value. Here we use the strain rate history shown in Fig. 3 as an example to analyze the radial inertia effect. As shown in Fig. 3, a small strain is accumulated during the ramping process of strain rate, $e_x(t) << 1$, Equation (37) thus becomes

$$\bar{\sigma}_r(t) = \frac{1}{8}\rho_0 \cdot a_0^2 \cdot \left[\ddot{\varepsilon}_x(t) + \frac{3}{2} \cdot \dot{\varepsilon}_x^2(t) \right] \tag{39}$$

During the strain rate ramping process shown in Fig. 3, the strain acceleration, $\ddot{\varepsilon}_x$, is on the order of 10^8 s^{-2} in magnitude, whereas $\dot{\varepsilon}_x^2$ is on the order of 10^7 s^{-2} in magnitude. Therefore, the second term in the bracket in Equation (37) is negligible. The radial-inertia-induced stress is simplified as

$$\bar{\sigma}_r(t) = \frac{1}{8}\rho_0 \cdot a_0^2 \cdot \ddot{\varepsilon}_x(t) \tag{40}$$

which is consistent with the equations obtained by Kolsky [15] and Forrestal et al. [16].

After a constant strain rate is achieved, the radial-inertia-induced stress (Equation (37)) is

$$\bar{\sigma}_r(t) = \frac{3}{16}\rho_0 a_0^2 \cdot \left[\frac{\dot{\varepsilon}_x}{1 - e_x(t)} \right]^2 \tag{41}$$

Equation (41) suggests that the amplitude of the radial-inertia-induced stress significantly increases with increasing specimen strain. Therefore, the radial inertia cannot be neglected when the specimen undergoes large deformation, even though a constant strain rate is achieved.

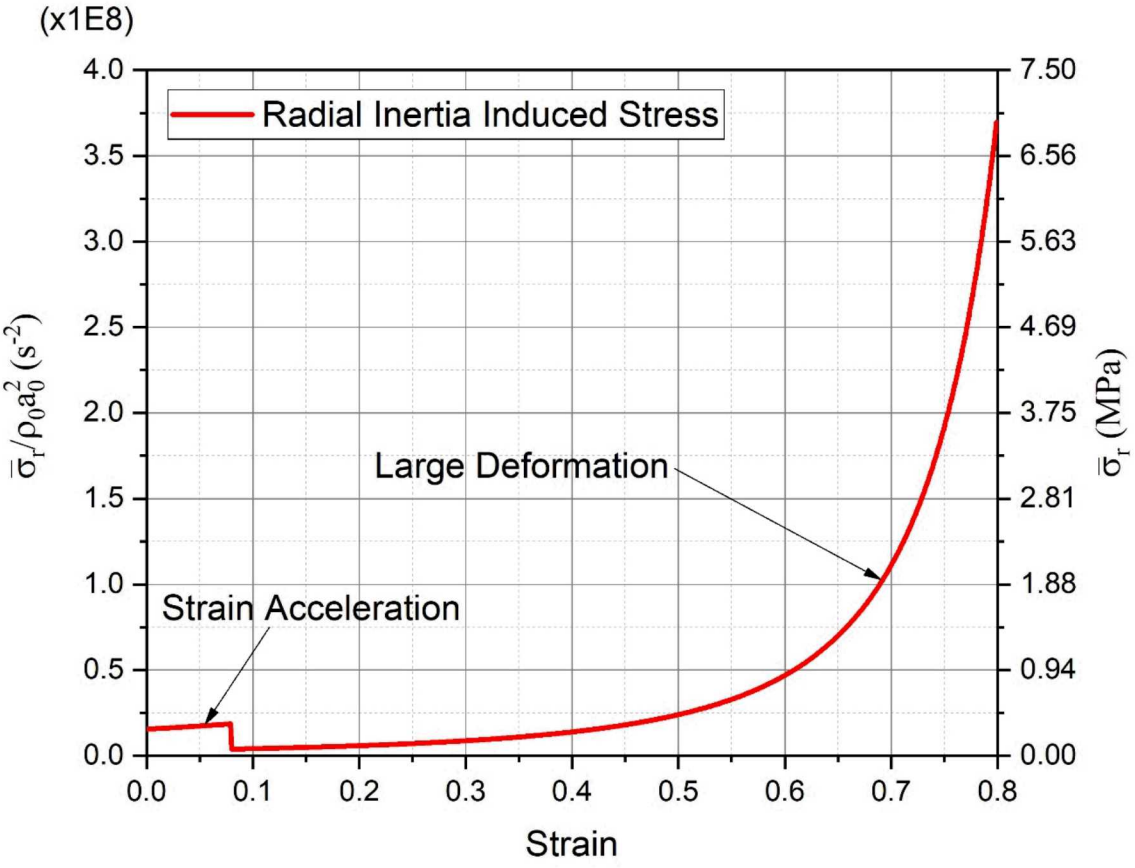

Figure 4. Radial inertia induced stress in an incompressible solid (gel rubber).

Considering a clear gel rubber with a density of 750 kg/m^3, the radial-inertia-induced stress (Equation (37)) and normalized stress (Equation (38)) in a solid specimen with 5-mm radius are shown in Fig. 4. As shown in Fig. 4, the strain acceleration dominates the radial inertia when strain is smaller than 0.08. Large-strain induced radial inertia becomes more and more significant with increasing strain, and drastically increases when specimen strain is larger than 0.5. The overall amplitude of the additional axial stress caused by the radial inertia is below 1 MPa when $\varepsilon < 0.6$ but could be a few MPas at larger strains. This amplitude would be negligible for some relatively hard rubber materials with higher strength, but not negligible for soft gel rubbers.

3.2 Radial inertia in a compressible solid with a constant Poisson's ratio

For a compressible solid with an arbitrary but constant Poisson's ratio, $0 \le \nu_0 < \frac{1}{2}$, we have

$$\frac{dr(t)}{r(t)} = -\nu_0 \frac{dl(t)}{l(t)} \tag{42}$$

Equation (42) gives the following solution,

$$\frac{r(t)}{r_0} = \left(\frac{l(t)}{l_0}\right)^{-\nu_0} \tag{43}$$

or

$$r(t) = r_0 \left(1 - e_x(t)\right)^{-\nu_0} \tag{44}$$

$$a(t) = a_0 \left(1 - e_x(t)\right)^{-\nu_0} \tag{45}$$

In addition, integrating Equation (16) yields

$$\rho(t) = \rho_0 \left(1 - e_x(t)\right)^{-(1-2\nu_0)} \tag{46}$$

Equation (31) is thus changed to

$$\sigma_r(r_0, t) = \rho_0 \cdot \frac{a_0^2 - r_0^2(t)}{2\left(1 - e_x(t)\right)^2} \cdot \left[\nu_0 \ddot{\varepsilon}_x(t) + \nu_0 \cdot (\nu_0 + 1) \frac{\dot{\varepsilon}_x^2(t)}{1 - e_x(t)} \right] \tag{47}$$

Substituting Equation (47) into (36) gives the average radial-inertia-induced stress,

$$\bar{\sigma}_r(t) = \frac{\rho_0 \cdot a_0^2}{4\left(1 - e_x(t)\right)^2} \cdot \left[\nu_0 \ddot{\varepsilon}_x(t) + \nu_0 \cdot (\nu_0 + 1) \frac{\dot{\varepsilon}_x^2(t)}{1 - e_x(t)} \right] \tag{48}$$

A normalized stress is expressed as

$$\frac{\bar{\sigma}_r(t)}{\rho_0 a_0^2} = \frac{1}{4(1 - \varepsilon_x(t))^2} \cdot \left[\nu_0 \ddot{\varepsilon}_x(t) + \nu_0 \cdot (\nu_0 + 1) \frac{\dot{\varepsilon}_x^2(t)}{1 - \varepsilon_x(t)} \right] \tag{49}$$

When $\nu = \frac{1}{2}$ for an incompressible solid, Equations (48) and (49) become Equations (37) and (38), respectively. For a given strain-rate history shown in Fig. 3, the radial-inertia-induced stress depends on the specimen strain and Poisson's ratio. The dependencies of radial inertia on specimen strain and Poisson's ratio are shown in Fig. 5. Figure 5 shows that a higher Poisson's ratio results in a more significant radial confinement effect to a specimen subjected to axial compression. The effect of Poisson's ratio on radial inertia is also nonlinear according to Equation (48) or (49). Note that the Poisson's ratio here is assumed to be constant, independent of specimen strain.

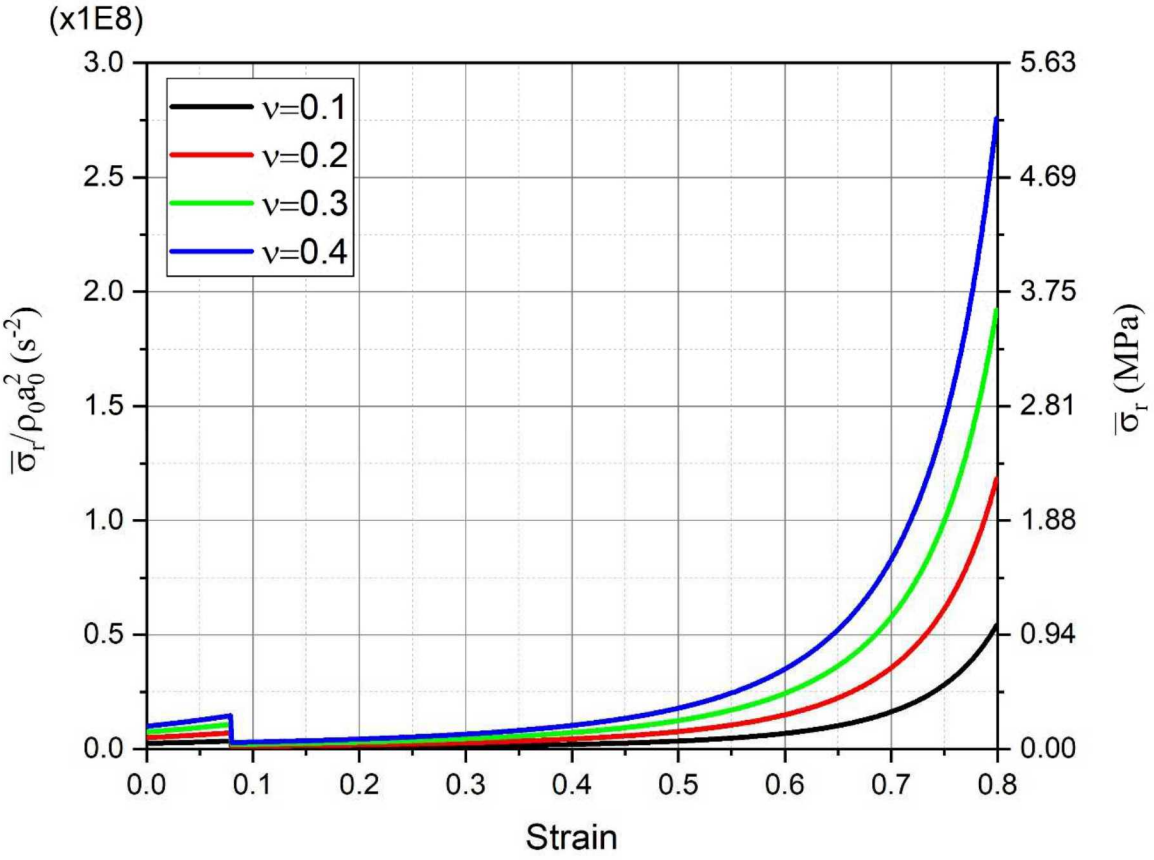

Figure 5. Poisson's ratio effect on radial-inertia-induced stress in a compressible solid specimen.

3.3 Radial inertia in a compressible solid with varying Poisson's ratio

As mentioned earlier, when a soft polymeric foam is subjected to dynamic compressive loading, the Poisson's ratio changes while the specimen is being deformed. However, such a variation of Poisson's ratio of polymeric foams has not yet been experimentally characterized. It is expected the Poisson's ratio does not significantly change before the foam is densified. However, the foam becomes nearly incompressible densification. Recently Sanborn and Song [25, 26] have

experimentally measured the Poisson's ratios of a hyperelastic silicone foam material under quasi-static and dynamic compressive loading. They found that the Poisson's ratio of the silicone foam followed Boltzmann function (Fig. 6),

$$\nu\left(e_x\right)=\frac{\nu_1-\nu_2}{1+\exp\left(\frac{e_x-e_{x0}}{\delta}\right)}+\nu_2 \tag{50}$$

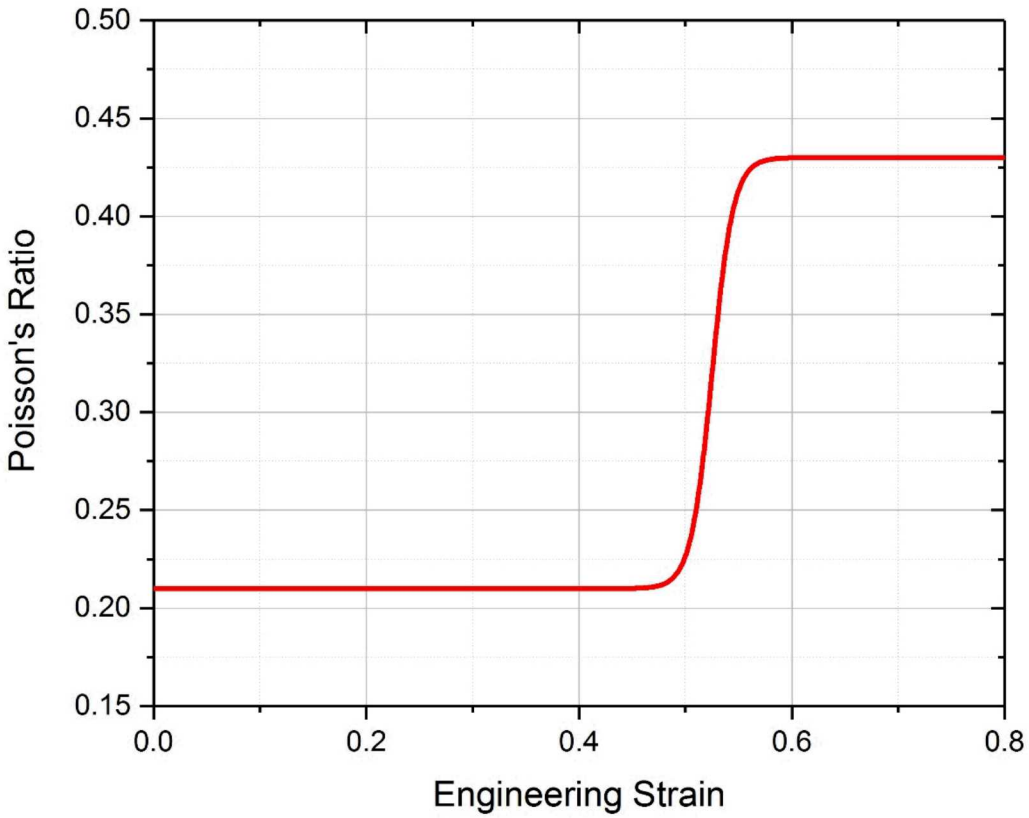

Figure 6. Dynamic Poisson's ratio of a silicone foam material.

where ν_1, ν_2, e_{x0}, and δ are constants. As shown in Fig.6, ν_1 and ν_2 represent Poisson's ratios before and after densification, respectively; e_{x0} could represent densification strain; and δ is the "width" of densification process. The dependency of Poisson's ratio on specimen strain is calculated as

$$\frac{d\nu(e_x)}{de_x} = \frac{\nu_2 - \nu_1}{\delta} \cdot \frac{\exp(\frac{e_x - e_{x0}}{\delta})}{\left[1 + \exp\left(\frac{e_x - e_{x0}}{\delta}\right)\right]^2} \tag{51}$$

Similar to Equation (42), we have

$$\frac{dr(t)}{r(t)} = -\nu(t)\frac{dl(t)}{l(t)} \tag{52}$$

Integrating Equation (42) yields

$$r(t) = C_1 \cdot e^{-\int \nu(t) d\ln l(t)} \tag{53}$$

where C_1 is constant and determined as

$$C_1 = r_0 \cdot e^{\int \nu(t) d\ln l(t)\big|_{l=l_0}} \tag{54}$$

Similarly, we have

$$a(t) = C_2 \cdot e^{-\int \nu(t) d\ln l(t)} \tag{55}$$

where

$$C_2 = a_0 \cdot e^{\int \nu(t) d\ln l(t)\big|_{l=l_0}} \tag{56}$$

From Equation (16), we have

$$\rho(t) = C_3 \cdot e^{-\int (1-2\nu(t)) d\ln l(t)} \tag{57}$$

where

$$C_3 = \rho_0 \cdot e^{\int (1-2\nu(t)) d\ln l(t)\big|_{l=l_0}} \tag{58}$$

Substituting Equations (53) – (58) into Equation (31) yields

$$\sigma_r(r_0,t) = \rho_0 \cdot \frac{a_0^2 - r_0^2}{2\left(1-e_x(t)\right)^2} \cdot \left[\begin{array}{l} \ddot{e}_x(t) \cdot \left(\nu_2 + \dfrac{\nu_1 - \nu_2}{1+\exp\left(\dfrac{e_x(t)-e_{x0}}{\delta}\right)} \right) \\ + \left(\nu_2 + \dfrac{\nu_1 - \nu_2}{1+\exp\left(\dfrac{e_x(t)-e_{x0}}{\delta}\right)} \right) \cdot \left(1+\nu_2 + \dfrac{\nu_1 - \nu_2}{1+\exp\left(\dfrac{e_x(t)-e_{x0}}{\delta}\right)} \right) \cdot \dfrac{\dot{e}_x(t)}{1-e_x(t)} \\ + \dot{e}_x(t) \cdot \dfrac{\nu_2 - \nu_1}{\delta} \cdot \dfrac{\exp\left(\dfrac{e_x(t)-e_{x0}}{\delta}\right)}{\left[1+\exp\left(\dfrac{e_x(t)-e_{x0}}{\delta}\right)\right]^2} \end{array} \right] \tag{59}$$

The average radial-inertia-induced stress is calculated with Equation (36) as

$$\bar{\sigma}_r(t)=\frac{\rho_0\cdot a_0^2}{4\left(1-e_x(t)\right)^2}\cdot\left[\begin{array}{l}\ddot{e}_x(t)\cdot\left(\nu_2+\dfrac{\nu_1-\nu_2}{1+\exp\left(\dfrac{e_x(t)-e_{x0}}{\delta}\right)}\right)\\ +\left(\nu_2+\dfrac{\nu_1-\nu_2}{1+\exp\left(\dfrac{e_x(t)-e_{x0}}{\delta}\right)}\right)\cdot\left(1+\nu_2+\dfrac{\nu_1-\nu_2}{1+\exp\left(\dfrac{e_x(t)-e_{x0}}{\delta}\right)}\right)\cdot\dfrac{\dot{e}_x^2(t)}{1-e_x(t)}\\ +\ddot{e}_x(t)\cdot\dfrac{\nu_2-\nu_1}{\delta}\cdot\dfrac{\exp\left(\dfrac{e_x(t)-e_{x0}}{\delta}\right)}{\left[1+\exp\left(\dfrac{e_x(t)-e_{x0}}{\delta}\right)\right]^2}\end{array}\right]$$

(60)

Here we use a silicone foam as an example. The silicone foam had a density of $\rho_0 = 649.1$ kg/m^3 and a porosity of 50%. The foam specimen had a diameter of 15 mm ($a_0 = 7.5$ mm). When the constants of Poisson's ratio are taken as $\nu_1 = 0.21$, $\nu_2 = 0.43$, $\varepsilon_{x0} = 0.525$, $\delta = 0.01$, Equation (60) becomes

$$\frac{\bar{\sigma}_r(t)}{\rho_0 a_0^2} = \frac{1}{4\left(1-e_x(t)\right)^2}\cdot\left[\begin{array}{l} \ddot{e}_x(t)\cdot\left(0.43-\dfrac{0.22}{1+\exp\left(\dfrac{e_x(t)-0.525}{0.01}\right)}\right) \\ +\left(0.43-\dfrac{0.22}{1+\exp\left(\dfrac{e_x(t)-0.525}{0.01}\right)}\right)\cdot\left(1.43-\dfrac{0.22}{1+\exp\left(\dfrac{e_x(t)-0.525}{0.01}\right)}\right)\cdot\dfrac{\dot{e}_x^2(t)}{1-e_x(t)} \\ +\dot{e}_x^2(t)\cdot\dfrac{22\cdot\exp\left(\dfrac{e_x(t)-0.525}{0.01}\right)}{\left[1+\exp\left(\dfrac{e_x(t)-0.525}{0.01}\right)\right]^2} \end{array}\right] \tag{61}$$

Based on the strain rate history shown in Fig. 3, the radial-inertia-induced stress (Equation (61)) in the silicone foam specimen is plotted in Fig. 7. Figure 7 shows a total radial-inertia-induced stress in three decomposed elements – strain acceleration induced radial inertia, large deformation induced radial inertia, and Poisson's ratio change induced redial inertia. Compared to Fig. 4, Poisson's ratio change generated not only a bump at 0.525 strain in the large deformation induced radial inertia (blue curve) but also an additional spike (green curve), then consequently a significant spike (3.57 MPa) in the total radial inertia induced stress (red curve). However, according to Equation (30), this Poisson's ratio induced radial inertia would be significantly reduced at lower strain rates. In other words, the Poisson's ratio-induced-radial inertia only becomes significant at very high strain rates.

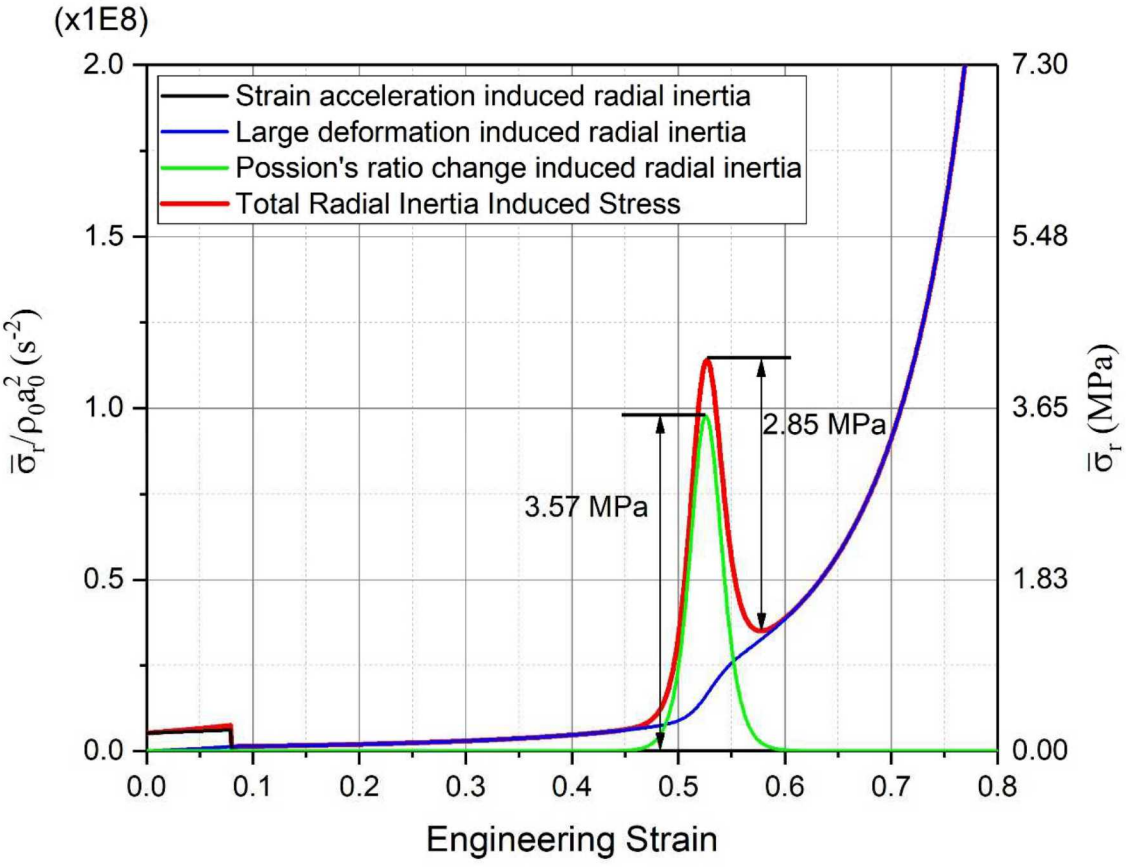

Figure 7. Radial-inertia-induced stress in a silicone foam material.

4. Experimental Verification

High rate compression experiments were carried out using a Kolsky compression bar (also called split Hopkinson pressure bar) shown in Fig. 1. The compression bar was made of aluminum 7075-

T6 and had incident and transmission bars that were 3.7 m and 2.7 m long, respectively, with a common diameter of 25.4 mm. In a Kolsky compression bar test, a striker bar was launched by a gas gun to impact the incident bar. An incident stress wave was generated and propagated in the incident bar. When the incident wave arrived at the specimen, due to mechanical impedance mismatch between the pressure bar and the specimen, part of it was reflected back into the incident bar as a reflected wave and the rest transmitted into the transmission bar while the specimen was compressed. The incident and reflected signals were recorded with the strain gages on the incident bar. The transmitted signal was recorded with the strain gages on the transmission bar. Due to the low transmitted force history of the foam specimen, semiconductor strain gages which have approximately 75 times greater sensitivity than resistor strain gages were used to measure the transmitted force. Quartz crystal force transducers were also installed to the specimen ends of the incident and transmission bars to directly record the forces at both ends of the specimen for force/stress equilibrium check [27]. Annealed copper pulse shapers were attached to the impact end of the incident bar to facilitate dynamic stress equilibrium and constant strain rate deformation in the sample.

Upon stress equilibrium, the strain rate, strain, and stress histories in the specimen were calculated with the following equations,

$$\dot{\varepsilon}(t) = -2\frac{C_b}{l_0}\varepsilon_r(t) \tag{62}$$

$$e(t) = -2\frac{C_b}{l_0}\int_0^t \varepsilon_r(t)dt \tag{63}$$

$$\sigma(t) = \frac{A_b}{A_s}E_b\varepsilon_t(t) \tag{64}$$

where ε_r and ε_t are the reflected and transmitted bar strains, respectively; C_b and E_b are elastic wave speed and Young's modulus of the bar material, respectively; A_b and A_s are cross sectional areas of the pressure bars and the specimen, respectively. The stress-strain response of the specimen material can be obtained from Equations (63) and (64) by eliminating the term of time.

In this study, a silicone foam with an open-cell structure [28] was dynamically characterized in compression with the Kolsky compression bar. The cells of the silicone foam were approximately 0.5 mm in size while the density of the foam was 649.1 ± 14.1 kg/m^3. The silicone foam was made into cylindrical samples with a diameter of 15 mm and a thickness of 2.85 mm. Silicone oil was applied to both ends of the silicone foam specimen to minimize the interfacial friction between the specimen and bar ends during dynamic compression.

The strain rate and stress histories of the silicone foam material were obtained with Equations (62) and (64) and plotted in Fig. 8. As shown in Fig. 8, the strain rate ramp time was approximately 100 μs from zero to a nearly constant value of ~4000 s^{-1}. The specimen stress gradually increased until a significant abnormal stress spike was observed when $t = 180$ μs. The stress then drastically increased after the spike. The dynamic compressive stress-strain curve of the silicone foam material is shown in Fig. 9. The specimen strain rate and stress histories (shown in Fig. 8) and the stress-strain curve (shown in Fig. 9) show that the silicone foam specimen was subjected to 1) strain acceleration before strain rate achieved a constant value; 2) large deformation (over 0.7 strain); and 3) drastic Poisson's ratio change before and after densification (Fig. 6). Therefore, in this case, the radial inertia in the silicone foam material consists all three elements as discussed earlier. Particularly, the significant stress spike observed in the stress history (Fig. 8) is very similar, in both shape and amplitude, to the spike shown in Fig. 7.

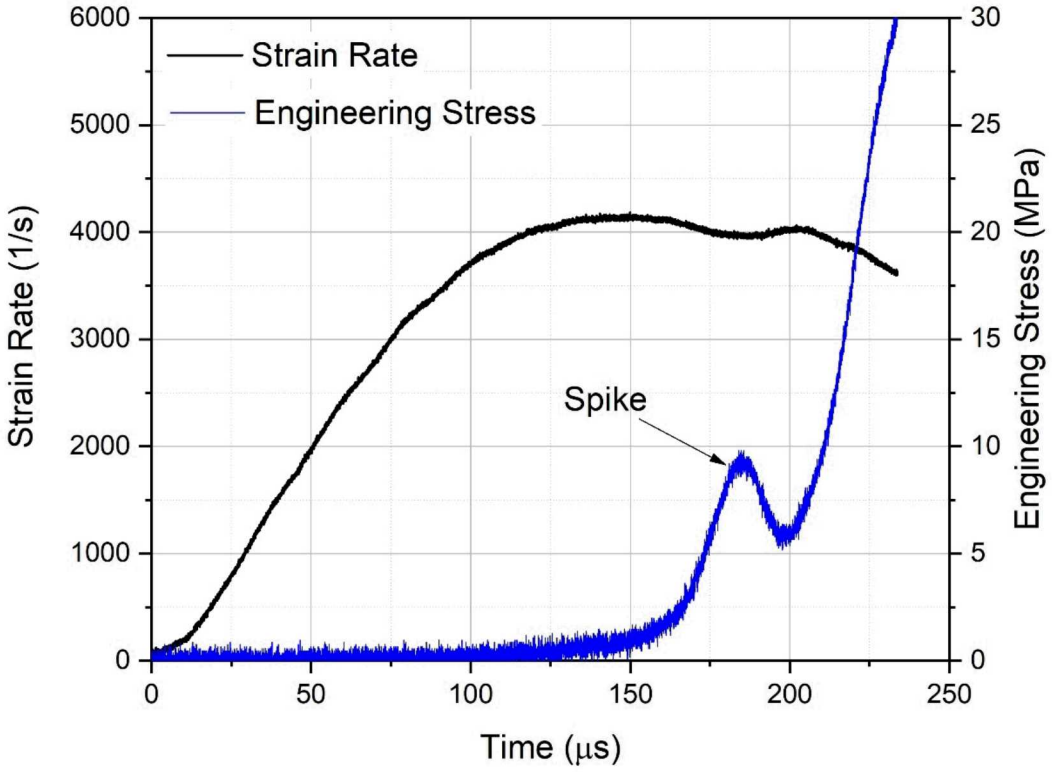

Figure 8. Actual strain rate and stress time histories in the silicone foam specimen.

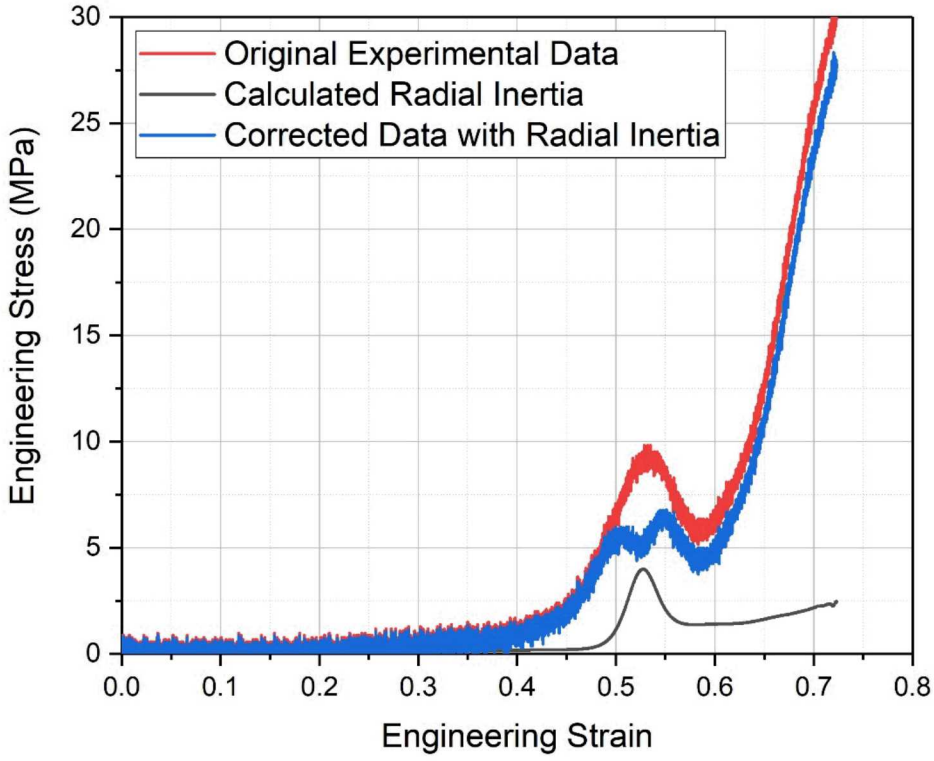

Figure 9. Dynamic compressive stress-strain curves directly measured from experiment and after correction with radial inertia.

Here Equation (61) and actual strain rate history shown in Fig. 8 was applied to calculate the total additional axial stress induced by radial inertia, the result of which is shown in Fig. 9. As seen in Fig. 9, the total additional radial-inertia-induced stress increases with specimen strain with a significant stress spike at the strain of 0.525, which is consistent with the spike location in the measured stress-strain response (red curve). The calculated radial-inertia-induced stress

was also deducted from the measured stress-strain response, the result of which is also shown in Fig. 9 (blue curve). The corrected stress-strain response roughly removed the spike but changed to a plateau. It is reasonable to conclude that the measured stress spike was caused by radial inertia due to significant Poisson's ratio change (dv/de). However, the Poisson's ratio function presented with Equation (50) and plotted in Fig. (6) was based on first-order Boltzmann approximation, which may not sufficiently represent the actual Poisson's ratio change across densification. This may not allow the radial-inertia-induced stress spike to be fully removed using numerical correction. A possible solution is to develop a higher order approximation of Poisson's ratio function that better captures the transition from compressible to nearly incompressible. This is expected to better numerically correct the radial inertia in the foam material. Another possible solution is to change the specimen geometry, i.e., using annular or tubular specimens as previously suggested by Song et al. [12] and Zhang et al. [21], to experimentally minimize the radial inertia. The radial inertial correction or minimization is still in progress and will be reported in the near future.

5. Conclusions

Radial inertia effects in a compressible solid subjected to dynamic compression were revisited, analyzed, and experimentally verified in this study. The radial inertia was generally induced by three different mechanisms – axial strain acceleration, large deformation, and Poisson's ratio change. The radial inertia in brittle materials with a constant Poisson's ratio is usually dominated by the axial strain acceleration. Large deformation results in more significant radial inertia in polymers subjected to large strains. Engineering materials usually possess a constant

Poisson's ratio such that the effect of Poisson's ratio change on radial inertia has been out of consideration. However, in a hyperelastic foam material, i.e. silicone foams in this study, the Poisson's ratio was drastically different before and after densification, which induced a third type of radial inertia. The radial inertia in foam materials consisted of all three elements, which consequently resulted in significant axial stress in addition to the actual intrinsic material response. Hence, new analysis was presented to account for these three factors. Using the new analytical technique on experimental data, the engineering stress-strain curve of a silicone foam specimen was numerically corrected to account for the radial-inertia-induced stress spike. However, refinements in both experimental measurement and numerical representation are needed to further improve the correction of radial inertia effect. Nonetheless, this work provided valuable insight into the effect of a variable Poisson's ratio on the stress-strain behavior, and provided a method to account for a changing Poisson's ratio to extract the intrinsic material behavior at high strain rates.

Acknowledgement

Sandia National Laboratories is a multimission laboratory managed and operated by National Technology and Engineering Solutions of Sandia, LLC, a wholly owned subsidiary of Honeywell International, Inc., for the U.S. Department of Energy's National Nuclear Security Administration under contract DE-NA0003525.

References

[1] Gibson, L.J. and Ashby, M.F., (1999) Cellular solids, structure and properties, 2nd edition, Cambridge University Press.

[2] Zhang, Z., Ming F., and Zhang, A., (2014) Damage characteristics of coated cylindrical shells subjected to underwater contact explosion, Shock and Vibration, 2014:763607.

[3] Rabe, J.A., Spells, S., Rasch, D.M., Homan, G.R., and Lee, C.L., (1981) Evaluation of silicone foam for flat plate solar collector insulation. Solar Energy Materials, 4:159-168.

[4] Blood, R.P., Ploger, J.D., Yost, M.G., Ching, R.P., and Johnson, P.W., (2010) Whole body vibration exposures in metropolitan bus drivers: a comparison of three seats. Journal of Sound and Vibration, 329:109-120.

[5] Song, B., Chen, W., and Lu, W.-Y., (2007) Compressive mechanical response of a low-density epoxy foam at various strain rates. Journal of Materials Science, 42:7502-7507.

[6] Song, B., Lu, W.-Y., Syn, C.J., and Chen, W., (2009) The effects of strain rate, density, and temperature on the mechanical properties of polymethylene diisocyanate (PMDI)-based rigid polyurethane foams during compression. Journal of Materials Science, 44:351-357.

[7] Song, B., Chen, W., Yanagita, T., and Frew, D.J., (2005) Confinement effects on the dynamic compressive properties of an epoxy syntactic foam. Composite Structures, 67:279-287.

[8] Song, B., Chen, W., Yanagita, T., and Frew, D.J. (2005) Temperature effects on dynamic compressive behavior of an epoxy syntactic foam. Composite Structures, 67:289-298.

[9] Chen, W., and Song, B., (2011) Split Hopkinson (Kolsky) Bar: Design, Testing and Applications. Springer, New York.

[10] Song, B., and Chen, W., (2005) Split Hopkinson pressure bar techniques for characterizing soft materials. Latin American Journal of Solids and Structures, 2:113-152.

[11] Song, B., Chen, W., and Jiang, X., (2005) Split Hopkinson pressure bar experiments on polymeric foams. International Journal of Vehicle Design, 37:185-198.

[12] Song, B., Chen, W.W., Ge, Y., Weerasooriya, T., (2007) Radial inertia effects in Kolsky bar testing of extra-soft materials. Experimental Mechanics, 47:659-670.

[13] Sanborn, B., Nie, X., Chen, W., and Weerasooriya, T., (2012) Inertia effects on characterization of dynamic response of brain tissue. Journal of Biomechanics, 45:434-439.

[14] Dharan, C.K.H., and Hauser, F.E., (1970) Determination of stress-strain characteristics at very high strain rates. Experimental Mechanics. September, 370-376.

[15] Kolsky, H., (1949) An investigation of the mechanical properties of materials at very high rates of loading. Proceedings of the Royal Society of London. B62:676-700.

[16] Forrestal, M.J., Wright, T.W., and Chen, W., (2007) The effect of radial inertia on brittle samples during the split Hopkinson pressure bar test. International Journal of Impact Engineering. 34:405-411.

[17] Li, Q.M., and Meng, H. (2003) About the dynamic strength enhancement of concrete-like materials in a split Hopkinson pressure bar test. International Journal of Solids and Structures. 40:343-360.

[18] Holland, C.C., and McMeeking, R.M., (2015) The influence of mechanical and microstructural properties on the rate-dependent fracture strength of ceramics in uniaxial compression. International Journal of Impact Engineering. 81:34-49.

[19] Rubin, M.B., and Rodríguez-Martínez, J.A. (2014) The effect of radial inertia on flow localization in ductile rods subjected to dynamic extension. International Journal of Impact Engineering. 69:157-164.

[20] Nishida, E.E. (2010) Distinguishing inertia effects from the intrinsic mechanical behavior of soft materials at high strain rates by Kolsky bar experiments. Master Thesis, Purdue University.

[20] Zhang, M., Li, Q.M., Huang, F.L., Wu, H.J., and Lu, Y.B., (2010) Inertia-induced radial confinement in an elastic tubular specimen subjected to axial strain acceleration. International Journal of Impact Engineering. 37:459-464.

[21] Warren, T.L., and Forrestal, M.J., (2010) Comments on the effect of radial inertia in the Kolsky bar test for an incompressible material. Experimental Mechanics. 50:1253-1255.

[22] Malvern, L.E., (1969) Introduction to the mechanics of a continuous medium. Prentice0Hall, Englewood Cliffs.

[23] Guduru, P.R., and Freund, L.B., (2002) The dynamics of multiple neck formation and fragmentation in high rate extension of ductile materials. International Journal of Solids and Structures. 39:5615-5632.

[24] Sanborn, B., and Song, B., (2018) Quasi-static and dynamic Poisson's ratio evolution of hyperelastic foams. 2018 SEM Annual Conference and Exposition on Experimental and Applied Mechanics, June 4-7, 2018, Greenville, SC, USA.

[25] Sanborn, B., and Song, B., (2018) Poisson's ratio of a hyperelastic foam under quasi-static and dynamic loading. International Journal of Impact Engineering (submitted).

[26] Casem, D., Weerasooriya, T., and Moy, P., (2005) Inertial effects of quartz force transducers embedded in a split Hopkinson pressure bar. Experimental Mechanics. 45:368-376.

[27] Lu, W.-Y., (2015) Compression of silicone foams. 2015 SEM Annual Conference and Exposition on Experimental and Applied Mechanics. June 8-11, 2015, Costa Mesa, CA, USA.